Bioconjugate Chemistry

pubs.acs.org/bc

Article

Synthetic Pept-Ins as a Generic Amyloid-Like Aggregation-Based Platform for *In Vivo* PET Imaging of Intracellular Targets

Maxime Siemons, Kaat Luyten, Ladan Khodaparast, Laleh Khodaparast, Joan Lecina, Filip Claes, Rodrigo Gallardo, Michel Koole, Meine Ramakers, Joost Schymkowitz,* Guy Bormans,* and Frederic Rousseau*

Cite This: *Bioconjugate Chem.* 2021, 32, 2052−2064

Read Online

ACCESS | Metrics & More | Article Recommendations | Supporting Information

ABSTRACT: Amyloid-like aggregation of proteins is induced by short amyloidogenic sequence segments within a specific protein sequence resulting in self-assembly into β-sheets. We recently validated a technology platform in which synthetic amyloid peptides ("Pept-ins") containing a specific aggregation-prone region (APR) are used to induce specific functional knockdown of the target protein from which the APR was derived, including bacterial, viral, and mammalian cell proteins. In this work, we investigated if Pept-ins can be used as vector probes for *in vivo* Positron Emission Tomography (PET) imaging of intracellular targets. The radiolabeled Pept-ins [^{68}Ga]Ga-NODAGA-PEG$_4$-vascin (targeting VEGFR2) and [^{68}Ga]Ga-NODAGA-PEG$_2$-P2 (targeting *E. coli*) were evaluated as PET probes. The Pept-in based radiotracers were cross-validated in a murine tumor and muscle infection model, respectively, and were found to combine target specificity with favorable *in vivo* pharmacokinetics. When the amyloidogenicity of the interacting region of the peptide is suppressed by mutation, cellular uptake and *in vivo* accumulation are abolished, highlighting the importance of the specific design of synthetic Pept-ins. The ubiquity of target-specific amyloidogenic sequence segments in natural proteins, the straightforward sequence-based design of the Pept-in probes, and their spontaneous internalization by cells suggest that Pept-ins may constitute a generic platform for *in vivo* PET imaging of intracellular targets.

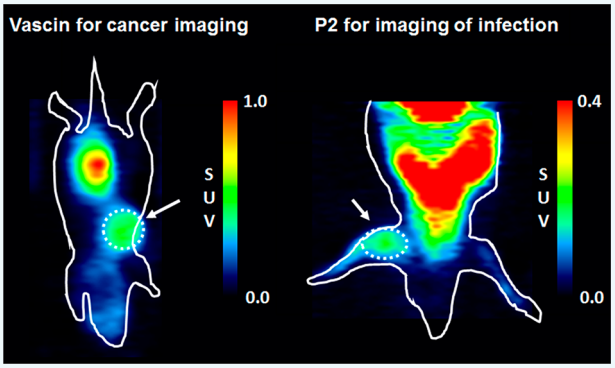

INTRODUCTION

Amyloid-like aggregation of proteins is induced by short amyloidogenic sequence segments within a protein sequence that are able to self-assemble into β-sheets, resulting in the characteristic cross-β structured spine of amyloid architecture[1,2] (Figure S1). In the aggregation seeding process, incorporation of nonhomologous sequences into the ordered and tightly packed in-register stacking of identical side chains is energetically disfavored.[3] Most of these amyloidogenic sequence segments are unique within their proteome, and proteins will usually only aggregate with identical proteins due to the sequence specificity of amyloid aggregation.[4] It has been established that synthetic amyloid peptides, based on an amyloidogenic fragment of a target protein (aggregation prone region or APR), could be exploited for specific *in vitro* protein detection in Western Blot using detection probes based on protein-specific APRs.[3] Moreover, grafted amyloid-motif antibodies or gamma bodies were developed in which APRs are grafted onto the complementarity-determining region of a single-domain antibody, generating conformation-specific antibody variants that recognize Aβ soluble oligomers and amyloid fibrils.[5] Hydrophobic peptidic probes based on the β-strand of transthyretin, were found to selectively detect misfolded transthyretin oligomers in plasma of hereditary amyloidosis patients.[6]

We recently developed a technology platform in which synthetic amyloid peptides containing an APR ("Pept-ins") are used to induce target-specific functional knockdown of the protein from which the APR was derived, and we delivered broad proof of concept in plants,[7] bacteria,[8,9] viruses,[10] and mammalian cells.[11] Given the well-established observation that the vast majority of proteins possess at least one APR,[12,13] these synthetic amyloid peptides potentially provide a generic platform for diagnostic and therapeutic applications, similar to antibodies and derivatives. In the current study, we investigated the potential of synthetic amyloid peptides as *in vivo* probes for Positron Emission Tomography (PET) by

Received: July 27, 2021
Revised: August 25, 2021
Published: September 6, 2021

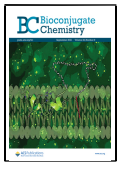

https://doi.org/10.1021/acs.bioconjchem.1c00369
Bioconjugate Chem. 2021, 32, 2052−2064

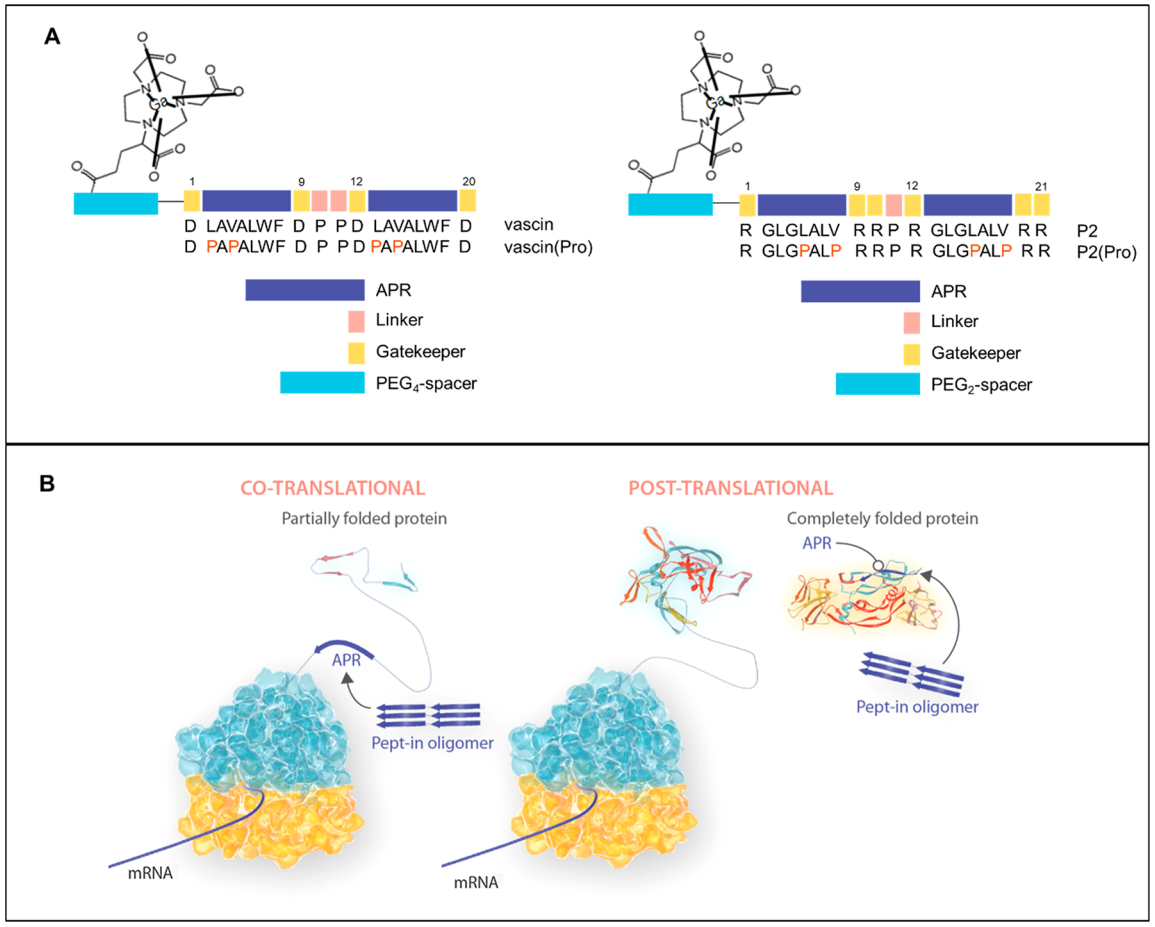

Figure 1. Design and intended mode of action of synthetic amyloid peptides for PET imaging. (a) Schematic representation of the design of [^{68}Ga]Ga-NODAGA-PEG$_4$-vascin and [^{68}Ga]Ga-NODAGA-PEG$_2$-P2. The positions of the APR, gatekeeper, and linker residues are shown, together with the sequence and the mutated residues of the proline variant in orange. Vascin and P2 are coupled at their N-terminus via a PEG spacer to the NODAGA chelator by which gallium is chelated. (b) Depiction of the hypothesized interaction mechanism of synthetic amyloid peptides, generically termed "Pept-ins", with their APR target. Instead of ligand−receptor interaction or epitope−antibody binding, Pept-ins interact with their target through their APR via a highly specific β-sheet aggregation interaction found in natural amyloid structures. The interaction can occur cotranslationally when the target protein is being translated on the ribosome and only partially folded, exposing the APR to the solvent. If the APR is on the surface of the protein, the APR can also be accessed post-translationally.

amyloid-mediated Pept-in/target interaction. Radionuclide imaging methods such as PET enable noninvasive imaging of diseases and biological processes, utilizing the high-affinity and high-selectivity interaction of radiolabeled compounds with their target *in vivo*.[14,15] We demonstrate that synthetic peptides carrying APRs of tumor-specific[12] or bacteria-specific targets[13,16] can be used for *in vivo* PET imaging. Importantly, as some amyloid aggregates are readily internalized by mammalian cells[17] and bacteria,[8] detection is not necessarily restricted to extracellular targets. The straightforward design and production of synthetic amyloid peptides by solid-phase peptide synthesis could potentially result in lower development and production costs compared to antibody (or derivatives) based radiotracers. Moreover, the intracellular targeting of synthetic amyloid peptides expands the range of possible disease targets beyond those currently accessible to antibodies and derivatives. The persistent accumulation of vascin in target tissue indicates the potential of Pept-ins labeled with α- or β-emitting radionuclides to be used for radionuclide therapy. This would extend the Pept-in technology to a theranostic approach in analogy to targeted radionuclide therapy with radiolabeled somatostatin analogues or PSMA targeting probes.[18,19]

RESULTS

Design of Synthetic Amyloid Radiotracers for *In Vivo* PET Imaging. To evaluate the applicability of synthetic amyloid peptides as PET radiotracers, we turned to previously developed peptides generically termed "Pept-ins", namely, the inhibitor of the mammalian Vascular Endothelial Growth Factor Receptor 2 (VEGFR2) called vascin[11] and an antimicrobial synthetic amyloid that induces massive aggregation in the Gram-negative bacteria *E. coli*, called P2[8].

The design and development of vascin and P2 were established elsewhere.[8,11] Both peptides consist of a tandem repeat of a target APR decorated by charged flanks and linked by a short peptide linker (Figure 1a). The aim of this design is to obtain amyloid forming peptides that assemble into metastable soluble oligomers, which are highly diffusible, cell penetrable and procure specificity by amyloid-mediated Pept-in/target interaction. In our design, two identical APRs[20] are connected by a rigid proline linker and are supercharged by placing aggregation gatekeepers, either negatively charged

https://doi.org/10.1021/acs.bioconjchem.1c00369
Bioconjugate Chem. 2021, 32, 2052−2064

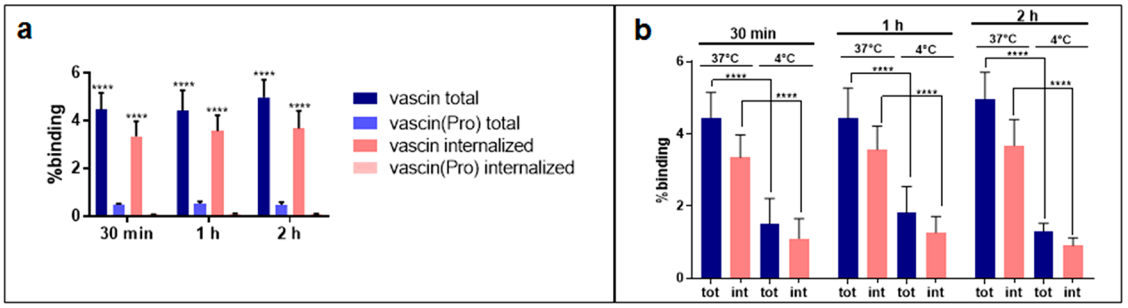

Figure 2. Vascin shows a high internalization compared to vascin(Pro). (a) HUVECs were incubated with [^{68}Ga]Ga-NODAGA-PEG$_4$-vascin (n = 6−9, 2−3 replicate experiments) or [^{68}Ga]Ga-NODAGA-PEG$_4$-vascin(Pro) (n = 6−12, 2−4 replicate experiments) at 37 °C for 30 min, 1 h, and 2 h. Values were calculated as % of total applied radioactivity associated with the cell fraction. Total binding is the sum of membrane-associated radioactivity (collected by glycine-HCl washing of cells) and internalized radioactivity. Data are expressed as mean ± SD. Statistical significance was calculated for vascin vs vascin(Pro) for each condition using unpaired Student's t test (**** $p < 0.0001$). (b) HUVECs were incubated with [^{68}Ga]Ga-NODAGA-PEG$_4$-vascin for 30 min, 1 h, and 2 h at 37 °C and at 4 °C (n = 6−9, 2−3 replicate experiments for each condition). Values were calculated as % of total applied radioactivity associated with the cell fraction. Data are expressed as mean ± SD. Statistical significance was calculated for each incubation time comparing total binding at 37 °C vs 4 °C and internalized fraction at 37 °C vs 4 °C using unpaired Student's t test (**** $p < 0.0001$).

aspartate or positively charged arginine residues, at the flanks of the APRs (Figure 1a), to obtain sufficient solubility of the resulting construct.[12,21,22] The mechanism of interaction of Pept-ins with their APR target is illustrated in Figure 1b. The interaction between the Pept-In and its target can occur cotranslationally, while the protein populates partially folded states in which the APR is exposed to the solvent (Figure 1b, cotranslational). On the other hand, if the APR resides near the surface of the folded protein, the APR can also be accessed post-translationally (Figure 1b, post-translational). Vascin is based on an APR derived from the VEGFR2-signaling peptide, and as expected, the interaction with VEGFR2 occurs intracellularly and cotranslationally.[11] In addition, for P2, experimental data strongly suggested that initial protein aggregation in response to P2 occurs cotranslationally.[8]

PET radiotracers are obtained by labeling compounds with positron-emitting radionuclides. Vascin and P2 were N-terminally conjugated to a PEG spacer followed by amino coupling to 1-(1-carboxy-3-carboxy-propyl)-4,7-(carboxy-methyl)-1,4,7-triazacyclononane (NODAGA) as a chelator for gallium-68 (Figure 1a), to obtain [^{68}Ga]Ga-NODAGA-PEG$_4$-vascin and [^{68}Ga]Ga-NODAGA-PEG$_2$-P2 (Figure S6). Control peptides were synthesized in which proline substitutions at different positions in the APRs were introduced to obtain proline (Pro) variants that served as control peptides, [^{68}Ga]Ga-NODAGA-PEG$_4$-vascin(Pro) and [^{68}Ga]Ga-NODAGA-PEG$_2$-P2(Pro) (Figure 1a). In these mutants, the overall hydrophobicity is largely conserved, but the β-sheet aggregation propensity is disrupted, to evaluate the amyloid-dependent specificity of the APR interaction with the target of [^{68}Ga]Ga-NODAGA-PEG$_4$-vascin(Pro) and [^{68}Ga]Ga-NODAGA-PEG$_2$-P2(Pro).

After chemical modification of vascin and P2 for radiolabeling, the conservation of the *in vitro* functional effect was assessed with ^{nat}Ga-labeled variants, which displayed similar target knockdown activity as unmodified peptides. In order to assess the conservation of the inhibitory effect of modified vascin on VEGFR2, extracellular signal-regulated kinase (ERK) phosphorylation was determined as described before.[11] Human umbilical vein endothelial cells (HUVECs) were treated overnight with unmodified vascin, [^{nat}Ga]Ga-NODAGA-PEG$_4$-vascin or [^{nat}Ga]Ga-NODAGA-PEG$_4$-vascin(Pro). HUVECs were then stimulated with VEGF and ERK phosphorylation was quantified. A similar decrease in total phosphorylated ERK was observed for ^{nat}Ga-labeled NODAGA-PEG$_4$-vascin compared to unmodified vascin as determined in the same assay (Figure S2). No decrease of phosphorylated ERK level was observed in cells treated with ^{nat}Ga-labeled NODAGA-PEG$_4$-vascin(Pro) (Figure S2).

P2 was previously shown to induce formation of large toxic inclusions in *E. coli* leading to proteostatic collapse and bacterial cell death.[23] In order to evaluate the conservation of this effect, ^{nat}Ga-labeled variants were used to determine the Minimum Inhibitory Concentration (MIC) against *E. coli* and construct time-killing curves with *E. coli* treated at MIC concentration. [^{nat}Ga]Ga-NODAGA-PEG$_2$-P2 had an MIC value of 50 μg/mL compared to 25 μg/mL for unmodified P2. Determination of the rate of bactericidal activity by time-killing experiments at MIC concentration showed a full bactericidal effect within 60 min. Formation of inclusion bodies was evaluated by staining the bacteria with the amyloid-specific dye p-FTAA and structured illumination microscopy (SIM). When the bacteria were treated at MIC concentration, intracellular inclusion bodies could be clearly observed (Figure S3a). p-FTAA specifically binds to amyloid-like aggregates,[24] validating the β-sheet-rich aggregated protein structure of the inclusion bodies. When analyzing these p-FTAA stained bacteria by Fluorescence Activated Cell Sorting (FACS) to study internalization and bacterial cell death, 98.8% of bacteria were positive for p-FTAA after 2 h, of which 55.4% were dead bacteria as indicated by propidium iodide (PI) staining (Figure S3b), which increased to 77.7% after 3 h (Figure S3c) and finally until 92.9% after 6 h (Figure S 3d). [^{nat}Ga]Ga-NODAGA-PEG$_2$-P2(Pro) induced neither aggregation nor bacterial cell death (Figure S3e).

To evaluate the capability of radiolabeled Pept-ins to engage intracellular targets, *in vitro* cell binding and internalization experiments were performed. HUVECs, which endogenously express VEGFR2, were incubated with [^{68}Ga]Ga-NODAGA-PEG$_4$-vascin and [^{68}Ga]Ga-NODAGA-PEG$_4$-vascin(Pro). Radiolabeled Vascin showed a significantly higher internalization compared to radiolabeled vascin(Pro) during the entire studied period (2 h), with barely any cellular uptake of radiolabeled vascin(Pro) (Figure 2a). It was shown earlier that

https://doi.org/10.1021/acs.bioconjchem.1c00369
Bioconjugate Chem. 2021, 32, 2052−2064

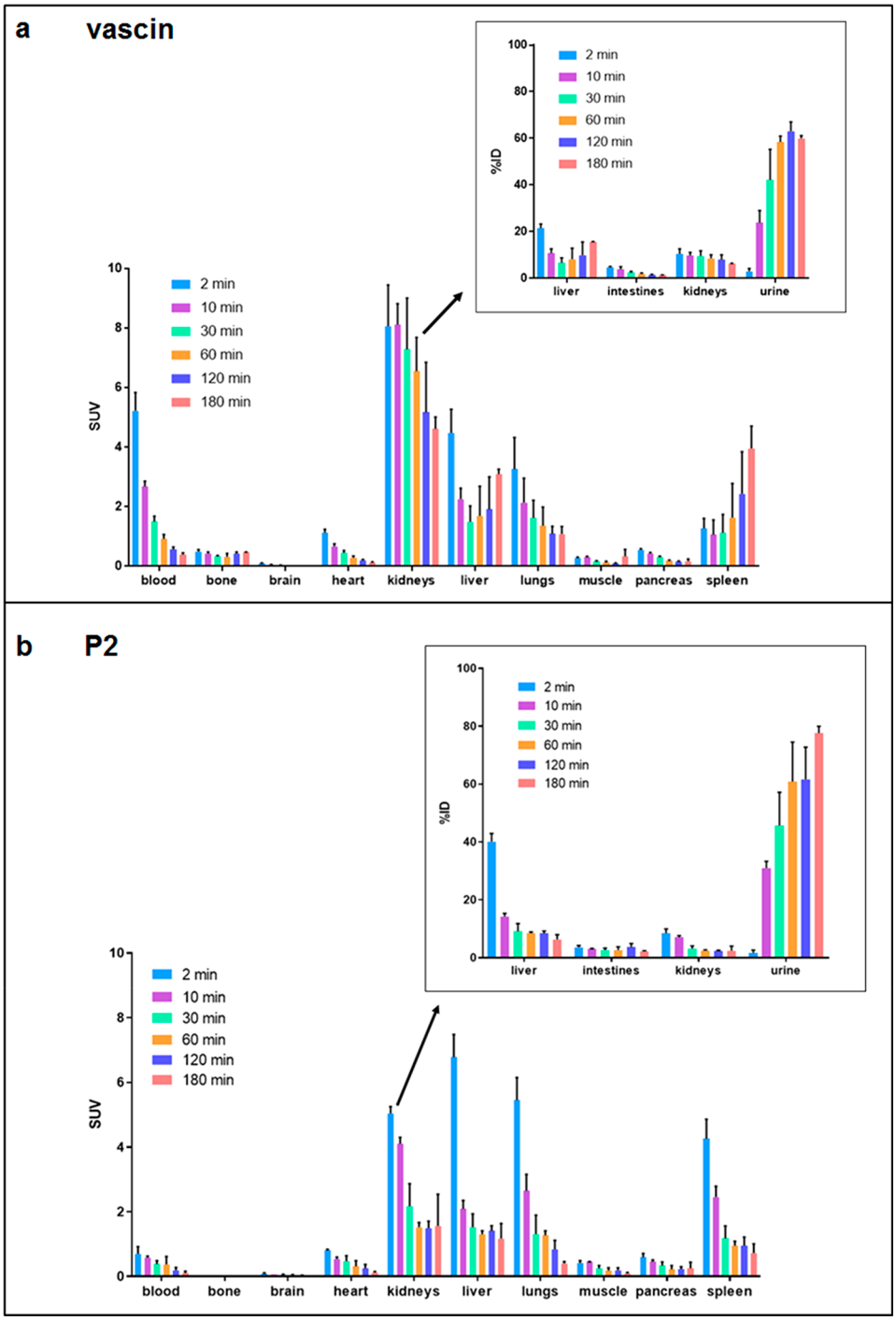

Figure 3. Vascin and P2 show a high urinary elimination and fast clearance from healthy tissue. (a) *Ex vivo* biodistribution study of [^{68}Ga]Ga-NODAGA-PEG$_4$-vascin in a mouse melanoma tumor model. Mice were euthanized between 2 min and 3 h after injection (n = 3−12 from 2 to 4 replicate experiments/time point). (b) *Ex vivo* biodistribution of [^{68}Ga]Ga-NODAGA-PEG$_2$-P2 in a mouse muscle infection model. Mice were euthanized between 2 min and 3 h after injection (n = 3−6/time point). The figures show the relative organ concentrations (SUV, standardized uptake value); the inset shows the general distribution (% ID, percentage injected dose) to provide information about the overall clearance of the peptide. Data are expressed as mean ± SD.

small aggregates (<500 nm in diameter) of peptides with the Pept-in format were internalized by mammalian cells through nonspecific endocytosis as part of the fluid phase.[17] When vascin was incubated with HUVECs at 4 °C, the observed uptake was significantly lower compared to 37 °C (Figure 2b), supporting that an active process such as endocytosis is responsible for the internalization of vascin. By mutation of residues in the APR to proline, the β-sheet aggregation propensity is abolished and it was observed that this leads to suppression of cellular uptake. This demonstrates that aggregate formation directly contributes to cellular uptake in eukaryotic cells and thus to the amenability of Pept-ins as radiotracers for PET imaging of intracellular targets.

For P2, supercharging with arginine residues is thought to promote cellular uptake into bacterial cells due to the strong electrochemical gradient of the bacterial membrane.[25] As a

https://doi.org/10.1021/acs.bioconjchem.1c00369
Bioconjugate Chem. 2021, 32, 2052−2064

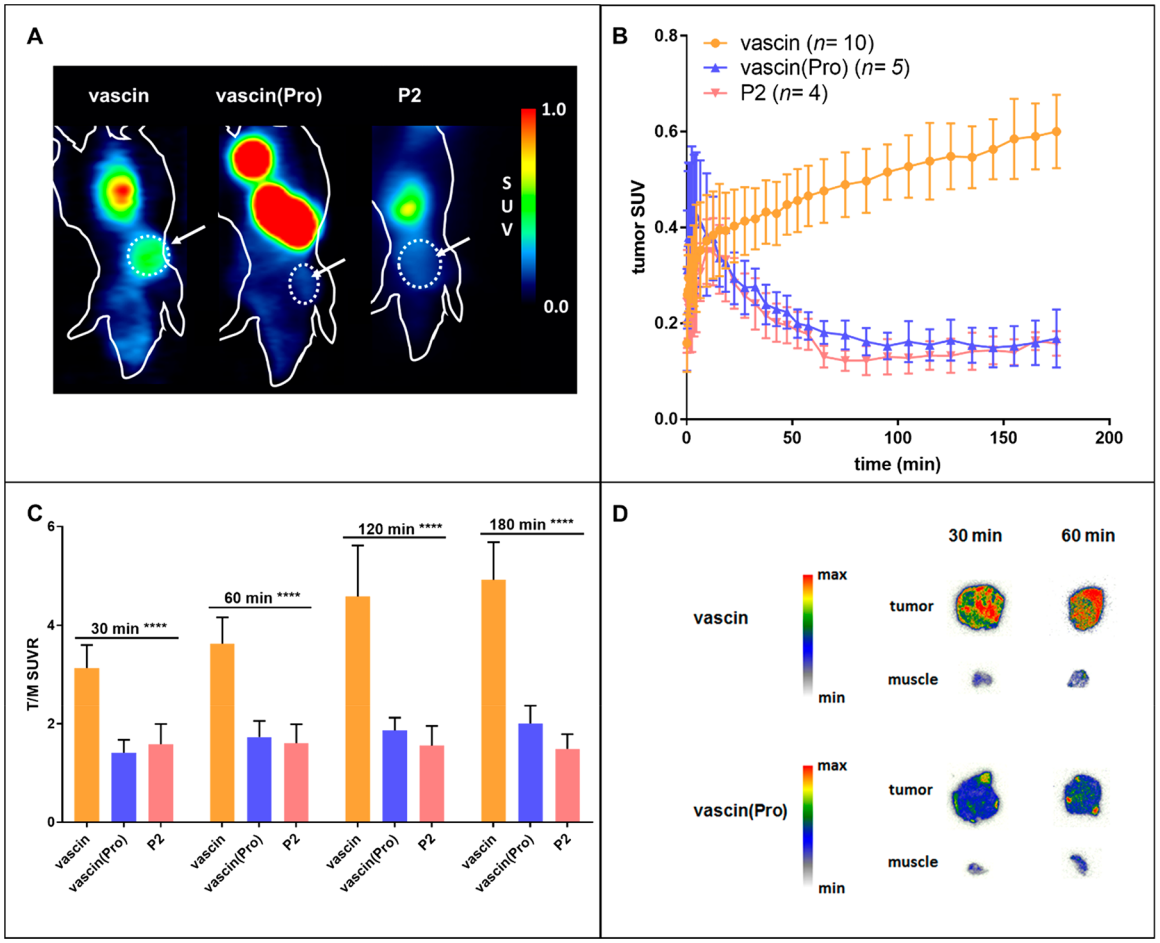

Figure 4. Specific *in vivo* accumulation of radiolabeled vascin at the tumor site in a mouse melanoma tumor model. (a) Representative whole-body coronal summed μPET images from 3 h dynamic scans in a mouse melanoma tumor model after injection of [^{68}Ga]Ga-NODAGA-PEG$_4$-vascin, [^{68}Ga]Ga-NODAGA-PEG$_4$-vascin(Pro), and [^{68}Ga]Ga-NODAGA-PEG$_2$-P2. Tumors are indicated by arrows. (b) μPET tumor SUV time−activity curves of [^{68}Ga]Ga-NODAGA-PEG$_4$-vascin, [^{68}Ga]Ga-NODAGA-PEG$_4$-vascin(Pro), and [^{68}Ga]Ga-NODAGA-PEG$_2$-P2. Data are expressed as mean ± SD from 6 replicate experiments for vascin and 2 replicate experiments for vascin(Pro) and P2. (c) μPET tumor-to-muscle SUV ratio bar plots of [^{68}Ga]Ga-NODAGA-PEG$_4$-vascin (n = 10 from 6 replicate experiments), [^{68}Ga]Ga-NODAGA-PEG$_4$-vascin(Pro) (n = 5 from 2 replicate experiments), and [^{68}Ga]Ga-NODAGA-PEG$_2$-P2 (n = 4 from 2 replicate experiments) at 30, 60, 120, and 180 min after tracer injection. Data are expressed as mean ± SD. Statistical significance was calculated for each time point using one-way ANOVA. (**** $p < 0.0001$). (d) Autoradiographs of representative transversal slices (50 μm) of snap-frozen tumor tissue and muscle tissue obtained from melanoma tumor mice that were euthanized 30 or 60 min after injection of [^{68}Ga]Ga-NODAGA-PEG$_4$-vascin (top panel) and [^{68}Ga]Ga-NODAGA-PEG$_4$-vascin(Pro) (lower panel).

result, both P2 as well as the nonaggregating P2(Pro) control are internalized by bacteria, but only P2 interacts with bacterial targets, induces intracellular bacterial protein aggregation, and accumulates in the bacterial cells.[8]

Synthetic Amyloid Radiotracers Display Favorable *in Vivo* Pharmacokinetics. A potential drawback of non-antibody proteins is that their plasma half-life is sometimes too short for diagnostic or therapeutic applications.[26] The plasma half-life needs to be sufficiently long to result in adequate tracer exposure of the target tissue, allowing for a sufficient fraction of the injected tracer to bind to its target *in vivo*. Radiolabeled peptides are mainly cleared from plasma via glomerular filtration in the kidneys often followed by reabsorption and retention of the radiolabel in the proximal tubular cells.

A high and persistent renal retention will lead to high radiation dose to the kidneys.[27,28] Substantial hepatic uptake of potential PET tracers for tumor imaging has to be avoided, since the liver is an important metastatic site for many malignancies, and hepatobiliary excretion will generate a high background in the whole abdominal region. Since [^{68}Ga]Ga-NODAGA-PEG$_4$-vascin would be useful to image VEGFR2 in tumor blood vessels through APR interaction, a functional angiogenesis model that is sensitive to inhibition of VEGFR2 was used for all *in vivo* characterization experiments.

The potential of [^{68}Ga]Ga-NODAGA-PEG$_2$-P2 for PET imaging of infection was evaluated in an *E. coli* muscle infection mouse model. To evaluate the pharmacokinetic properties of [^{68}Ga]Ga-NODAGA-PEG$_4$-vascin and [^{68}Ga]Ga-NODAGA-PEG$_2$-P2, biodistribution in mice between 2 min and 3 h after intravenous injection was determined. The biodistribution data showed moderate uptake of radiolabeled vascin (n = 3−12/time point) in kidney, spleen, and liver and fast blood clearance and a high urinary elimination (Figure 3a). Minor accumulation was observed in spleen and liver from 60 min onward (Figure 3a).

For radiolabeled P2, moderate uptake in kidneys, liver, and spleen, rapid blood clearance, and urinary excretion was

https://doi.org/10.1021/acs.bioconjchem.1c00369
Bioconjugate Chem. 2021, 32, 2052−2064

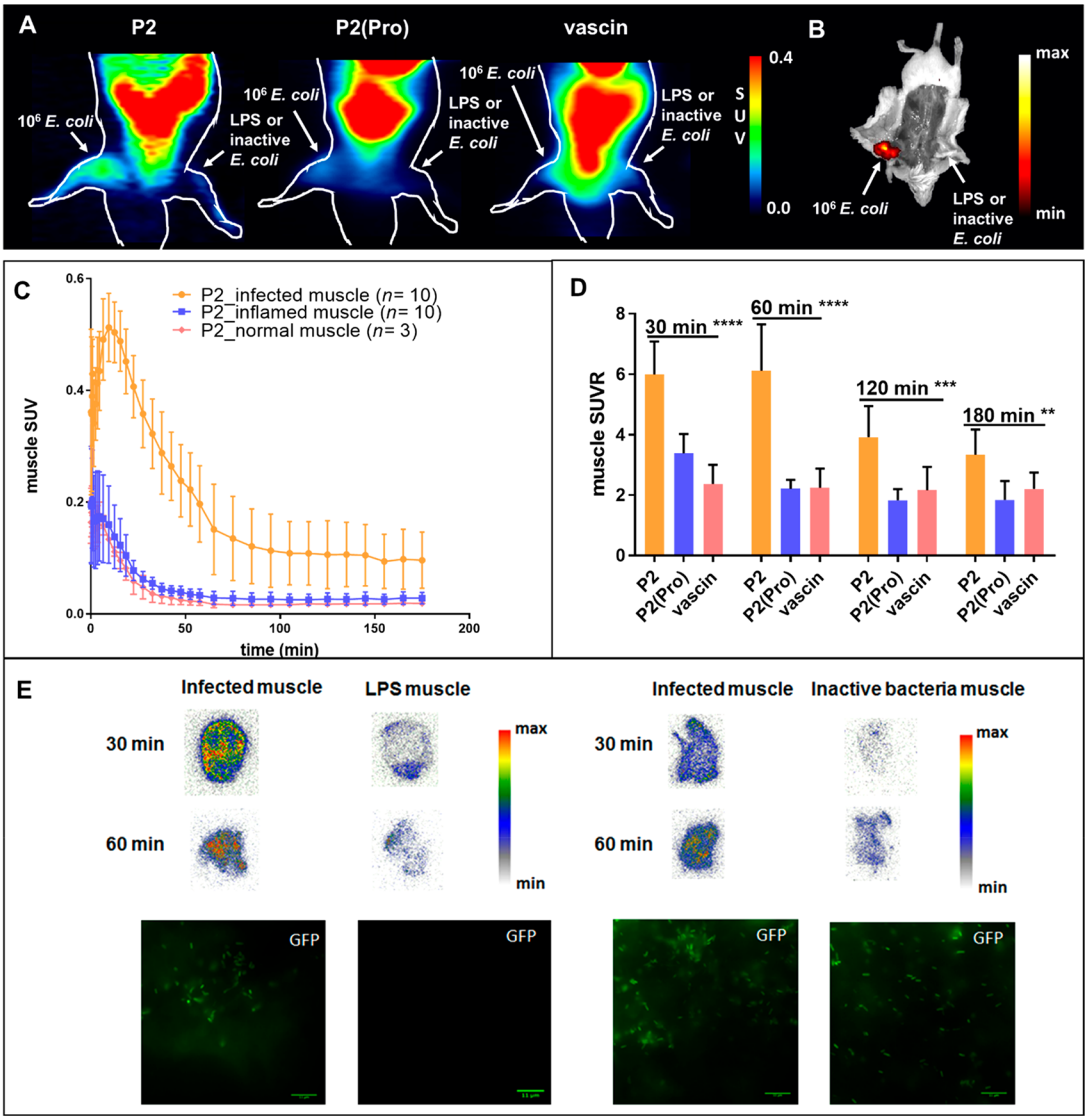

Figure 5. Specific *in vivo* accumulation of radiolabeled P2 at the *E. coli* infection site in a mouse muscle infection model. (a) Representative whole-body coronal summed μPET images from 3 h dynamic scans in a foreleg muscle infection model after injection of [^{68}Ga]Ga-NODAGA-PEG$_2$-P2, [^{68}Ga]Ga-NODAGA-PEG$_2$-P2(Pro), and [^{68}Ga]Ga-NODAGA-PEG$_4$-vascin. The image shown for P2 and P2(Pro) is obtained from the inactive bacteria model and for vascin from the LPS-model. (b) Whole-body fluorescence imaging of GFP-expressing *E. coli* in a foreleg muscle infection model. Inactivated *E. coli* have too low remaining GFP-expression to be detected by whole-body fluorescence imaging. The image shown is obtained from the LPS model. (c) μPET tumor SUV time−activity curves of [^{68}Ga]Ga-NODAGA-PEG$_2$-P2 in a foreleg muscle infection model in infected muscle, in inflamed muscle, and in normal muscle. The uptake in LPS-injected and heat-shock-treated bacteria-injected muscle were pooled together as "inflamed muscle". Data are expressed as mean ± SD from 2 to 6 replicate experiments per peptide. (d) μPET muscle SUVR at different time points for [^{68}Ga]Ga-NODAGA-PEG$_2$-P2 (n = 10 from 6 replicates), [^{68}Ga]Ga-NODAGA-PEG$_2$-P2(Pro) (n = 6 from 3 replicate experiments), and [^{68}Ga]Ga-NODAGA-PEG$_4$-vascin (n = 4 from 2 replicate experiments). Data are expressed as mean ± SD. Statistical significance was calculated for each time point using one-way ANOVA (** $p < 0.01$, *** $p < 0.001$, **** $p < 0.0001$). (e) Autoradiography of representative transversal slices (50 μm) of infected muscle tissue, LPS injected muscle (left panel), and inactive bacteria-injected muscle (right panel) obtained from mice that were euthanized 30 min and 60 after injection of [^{68}Ga]Ga-NODAGA-PEG$_2$-P2. Depicted slices per time point in each panel originate from the same mouse. Tissue slices (5 μm) were imaged using SIM, in which the figures display the signal from the GFP-expressing bacteria. Scale bars are 11 μm.

observed (n = 3−6/time point) (Figure 3b). Radiolabeled P2 was efficiently cleared from all the major organs, indicating low background, so that it can potentially be used for imaging infections in a wide range of tissues.

To summarize, no problematic accumulation of radiolabeled Pept-ins in healthy tissue was observed combined with efficient plasma clearance. *Ex vivo* plasma radiometabolite analysis of [^{68}Ga]Ga-NODAGA-PEG$_4$-vascin and [^{68}Ga]Ga-NODAGA-PEG$_2$-P2 by radioHPLC indicated a relatively slow metabolism, considering their peptidic nature (Figure S7). A substantial fraction of activity eluted in the beginning of the HPLC runs, which most likely correspond to polar small radiolabeled fragments.

Synthetic Amyloid Radiotracers Display Specific *in Vivo* Accumulation in Disease Models. The ability of radiolabeled vascin to image VEGFR2 in tumors through APR interaction was evaluated in a functional angiogenesis model that is sensitive to inhibition of VEGFR2 *in vivo*. This model

https://doi.org/10.1021/acs.bioconjchem.1c00369
Bioconjugate Chem. 2021, 32, 2052−2064

was generated by subcutaneous injection of B16 melanoma cells into the dorsal flank of C57BL/6 inbred mice, in which the tumor growth is effectively decreased by VEGFR2-specific inhibition.[29] Dynamic 3 h μPET imaging in the mouse model was performed after IV injection of [^{68}Ga]Ga-NODAGA-PEG$_4$-vascin, the proline-mutated version [^{68}Ga]Ga-NODAGA-PEG$_4$-vascin(Pro) and [^{68}Ga]Ga-NODAGA-PEG$_2$-P2 (n = 4−10/peptide), the latter two tracers were used as controls.

PET images (Figure 4a) and tumor time−activity curves (Figure 4b) of [^{68}Ga]Ga-NODAGA-PEG$_4$-vascin demonstrated significantly higher tumor uptake compared to both radiolabeled control peptides. Foreleg muscle was used to determine the tumor-to-muscle standardized uptake value (SUV) ratio (T/M SUVR) which was also found to be significantly higher than for both control radiopeptides at all studied time points (Figure 4c). When the β-sheet structure breaking proline was inserted into the APR region (radiolabeled vascin(Pro)), the tumor accumulation was abolished. In addition, radiolabeled P2 was studied as a control in the melanoma tumor model mice to exclude the aspecific enhanced permeability and retention (EPR) effect[30] as the potential mechanism of *in vivo* accumulation of Pept-in self-aggregates. Again, no *in vivo* tumor accumulation was observed after injection of the radiolabeled P2 (Figure 4b and c). These data thus suggest a specific aggregation-dependent interaction of radiolabeled vascin with VEGFR2 in the tumor blood vessels. *Ex vivo* autoradiography studies on snap-frozen tumor and muscle tissue confirmed the accumulation of radiolabeled vascin in the tumor (Figure 4d) and showed high intratumoral variability.

A key challenge in PET imaging of bacterial infection is to develop probes that are specific for bacteria and are able to distinguish bacterial infection from sterile inflammation.[31] PET tracers clinically used for infection imaging such as 2-[^{18}F]fluoro-2-deoxy-D-glucose ([^{18}F]FDG) and [^{67}Ga]Ga-citrate[32] employ retention mechanisms that are also upregulated in inflammation or cancer, and thus lack specificity. Radiolabeled P2 has the potential to image bacteria with high specificity, since mammalian cells do not express its bacterial targets, as it was previously shown that P2 preferentially accumulates in *E. coli* as observed in a coculture of mammalian (HeLa) cells and *E. coli*.[8] Hence, we studied PET imaging of infection with [^{68}Ga]Ga-NODAGA-PEG$_2$-P2 in an *E. coli* muscle infection model. Infection was induced by inoculation of green fluorescent protein (GFP)-expressing *E. coli* in the left foreleg or hind leg muscle, whereas in the contralateral muscle, lipopolysaccharide (LPS) or heat-inactivated *E. coli* were injected to induce sterile inflammation. Mice were anaesthetized using isoflurane, and the tracer was injected via a tail vein 24 h after injection of bacteria into muscle. The proline-mutated version [^{68}Ga]Ga-NODAGA-PEG$_2$-P2(Pro) and [^{68}Ga]Ga-NODAGA-PEG$_4$-vascin were used as control tracers. Dynamic 3 h μPET imaging followed by quantification of uptake in the muscle tissues were performed (n = 3−6/peptide). After the PET imaging experiments, whole-body fluorescence imaging was performed to validate the presence of bacteria, which was followed by dissection of muscle tissue and bacteria culturing to estimate the number of colony-forming units (CFU). PET imaging with [^{68}Ga]Ga-NODAGA-PEG$_2$-P2 visualized the infection sites and distinguished between infected and inflamed muscle, both the foreleg model and the hind leg model of muscle infection (Figures 5a and S4). [^{68}Ga]Ga-NODAGA-PEG2-P2(Pro) and [^{68}Ga]Ga-NODAGA-PEG$_4$-vascin on the other hand were not able to distinguish infected from inflamed muscle. There was no difference in PET image contrast between LPS-injected or heat-inactivated *E. coli*-injected muscle for all tested radiolabeled peptides. After PET imaging, whole-body fluorescence imaging (Figures 5b and S4) visualized the presence of GFP-labeled bacteria, and CFU counting of homogenized muscle tissue estimated the presence of 10^6 CFU *E. coli* in infected foreleg muscle in all executed experiments. Time−activity curves demonstrated high uptake of radiolabeled P2 at the infection site. In contrast, radiolabeled P2 efficiently cleared from both LPS-injected and inactivated bacteria-injected control muscle (Figure 5c). The uptake in control muscle injected with LPS or heat-inactivated bacteria was similar to the uptake in unmanipulated muscle (Figure 5c). Furthermore, infected muscle-to-inflamed muscle SUV ratios (muscle SUVR) were constructed (Figure 5d). The presence of β-breaking proline mutations in radiolabeled P2(Pro) significantly reduced radiotracer accumulation at the infection site compared to radiolabeled P2 (Figure 5d). In previous studies, fluorescently labeled P2(Pro) was observed to be internalized by bacteria but without induction of endogenous bacterial protein aggregation or lethal inclusion body formation.[8] Radiolabeled vascin was used as a cross-validation control to exclude nonspecific EPR effect[30] accumulation of peptide self-aggregates as a mechanism of *in vivo* accumulation at the target site (Figure 5d). Muscle SUVR of radiolabeled vascin were significantly lower than P2 muscle SUVR (Figure 5d). These data indicate bacteria-specific targeting of radiolabeled P2. To confirm the induction of inflammation in the LPS-injected and the inactive bacteria-injected control muscle, a static [^{18}F]FDG μPET was acquired 30 min post-injection. [^{18}F]FDG is known not to distinguish infection from inflammation.[33,34] The inflamed muscle tissue in the LPS model and the inactive bacteria-containing muscle were clearly visualized by [^{18}F]FDG, with a muscle SUVR in the LPS model of 1.0 ± 0.2 (n = 3) and 1.4 ± 0.5 (n = 4) in the inactive bacteria model (Figure S5) indicating a similar accumulation of [^{18}F]FDG in both inflamed and infected muscle. The specific accumulation of radiolabeled P2 at infection foci was validated by *ex vivo* autoradiography studies (Figure 5e). After the autoradiography experiments, structured illumination microscopy (SIM) confirmed the presence of bacteria in the infected muscle slices and the absence in the LPS muscle slices (Figure 5e). In the inactive bacteria muscle slices, the presence of heat-inactivated bacteria was shown (Figure 5e).

DISCUSSION

This work shows that short synthetic amyloidogenic peptides can be designed for specific *in vivo* PET imaging of intracellular targets. The rationale of this new concept was based on the following properties of amyloids: (a) their ability to spontaneously internalize into cells after peptide self-aggregate formation; (b) their specificity for protein APRs based on a specific amino acid sequence. Instead of ligand−receptor interaction or epitope−antibody binding, Pept-ins interact selectively with their target APR via highly specific β-sheet aggregation interactions also found in natural amyloid structures. Control studies with proline APR-mutated Pept-ins and cross-validation of both radiolabeled vascin and P2 in different disease models strongly suggest that the amyloid-based binding of Pept-ins is responsible for the observed *in vivo* target-specific uptake.

https://doi.org/10.1021/acs.bioconjchem.1c00369
Bioconjugate Chem. 2021, 32, 2052−2064

Quantifying VEGFR expression by noninvasive molecular imaging can be useful in the selection of cancer patients potentially benefiting from antiangiogenic therapy and would allow monitoring of therapeutic responses in real-time in a noninvasive way. Several preclinical and clinical approaches have been studied for imaging tumor angiogenesis, but to date, unfortunately none has emerged as a gold standard for monitoring antiangiogenic therapy or made it to approval for clinical use.[35,36] PET imaging with radiolabeled VEGFR2-targeting vascin provided good tumor SUV and T/M SUVR values compared to several other tumor-targeting peptidic tracers[37−39] and VEGF-pathway targeting recombinant protein tracers.[40−42] This could be due to the persisting accumulation in the tumor site over the 3 h scanning period. Despite a relatively high urinary excretion, the SUV in kidney (around 4.5 at 180 min) and liver (around 3 at 180 min) are higher than tumor uptake (around 0.6 at 180 min). Several published peptide-based radiotracers and VEGF-pathway targeting tracers also showed higher kidney and/or liver retention compared to their tumor uptake.[40−43] Some other reported tracers, however, showed more favorable pharmacokinetic properties.[37,44−47]

Despite many efforts, there is still an unmet need for infection-specific molecular imaging probes.[32,33] PET imaging with radiolabeled P2 demonstrated that antibacterial Pept-ins could provide an interesting new approach for molecular imaging of infectious disease. P2 allowed to detect as few as 10^6 CFUs of *E. coli*, a condition mimicking early-stage infection in a clinical setting.[48−50] P2 PET inflamed vs infected muscle SUVR ranged from about 6 at 60 min after injection, to about 3 at 180 min after injection, and compared with its *in vivo* detection of as few as 10^6 CFUs of *E. coli*, radiolabeled P2 performs similarly compared to recently reported promising tracers like radiolabeled sugars,[49−54] 2-[^{18}F]F-PABA,[55] ^{68}Ga-labeled UBI-29-41[56] or [^{18}F]fluoropropyl-trimethoprim.[57] Moreover, radiolabeled P2 was injected into the melanoma tumor model and showed a lack of tumor accumulation, which confirms infection-specific uptake rather than nonspecific EPR-driven uptake. Although P2 is efficiently excreted via the urine, the SUV in kidneys (around 1.5 at 180 min) and liver (around 1 at 180 min) are not insignificant compared with infected muscle (maximum SUV 0.5 at 10 min and 0.3 at 30 min), but lower compared to kidneys and liver retention of radiolabeled vascin. Radiolabeled sugars showed lower kidney and liver uptake than P2,[49,53,54,58] but compared to other peptidic probes for imaging of infection such as ^{68}Ga-labeled UBI-29-41,[59] kidney retention was much lower for P2.

Previous therapeutic studies in mice were performed with 10 mg/kg Pept-in doses[8,11] (∼100 nmol Pept-in administered to a 20 g mouse), these low mass doses (∼0.1 nmol Pept-in administered to a 20 g mouse) of radiolabeled Pept-ins *in vivo* were not previously explored. The amyloid aggregation process is concentration-dependent, but nevertheless the specificity of the amyloid interaction of Pept-ins appeared to be preserved at this low dose range. One of the strengths of the Pept-in technology is that the peptide sequence is based on that of the target protein, providing an easy rational design approach using the TANGO algorithm[20] to identify protein specific APRs upfront. Pept-ins are small peptides (consisting of 5 to 20 amino acids) that are readily obtained by solid-phase chemistry. Both P2 and vascin engage their target in the intracellular environment, profoundly extending the range of imaging disease markers beyond extracellular targets. It was previously demonstrated that Pept-ins showed potential as therapeutic agents, since vascin could inhibit VEGF-dependent tumor growth in a mouse melanoma tumor model[11] and P2 showed antibacterial efficacy in a mouse bladder infection model.[8] Another study showed the capability to design virus-specific amyloids and demonstrated therapeutic intervention in an influenza A mouse model.[10] The proof-of-concept study described in this work contributes to the foundation of a new generic platform for diagnostics and therapeutics based on Pept-ins, considering that the majority of proteins contain short amyloidogenic segments in their sequence of which the majority are unique within a proteome.[12,13] Considering the persisting accumulation in tumor tissue observed in the PET time−activity curves of vascin, Pept-ins labeled with α- or β-emitting radionuclides may also have potential for radionuclide therapy. For PET imaging, future research efforts should focus on improvement of pharmacokinetic properties of the Pept-in probes and broadening the scope of this exciting new platform. For a theranostic approach, next to the high target-to-background activity ratio of vascin, it should be investigated if there is also a sufficiently long residence time in the target tissue.

EXPERIMENTAL PROCEDURES

The methods used for the peptide synthesis, synthesis of the radiolabeled peptides, and *ex vivo* plasma radiometabolite analysis have been described in the Supporting Information. All animal procedures were approved by the local University Ethics Committee for Animals.

ERK Assay. Functionality of modified vascin was evaluated by an extracellular signal-regulated kinase (ERK) ERK1/2 assay performed on HUVECs as described previously.[11] Cells were treated overnight with 20 μM of peptide solution and then stimulated with 25 ng/mL recombinant VEGF for exactly 5 min at 37 °C. After this process, the cells were washed twice with ice-cold phosphate buffered saline (PBS) and lysed. Quantification of ERK1/2 phosphorylation and total ERK1/2 was done using the ERK1/2 mesoscale discovery ELISA kit (MSD ELISA) according to the supplier protocol. The wells of the plate included in the kit are precoated with capture antibodies for phosphorylated ERK1/2 and total ERK1/2. To summarize the supplier protocol, before starting the assay the wells were washed with 300 μL Tris wash buffer (35:315 Tris wash buffer 10×/deionized water v/v). Next, 150 μL blocking solution (30 mg Blocker A/mL 1× Tris wash buffer) was added to each well. After incubation of this solution for 1 h, together with vigorous shaking at room temperature, the wells were washed with 300 μL Tris wash buffer. Lysate samples were added (25 μL) and incubated for 3 h with vigorous shaking at room temperature. The wells were washed with 300 μL Tris wash buffer, and a detection antibody solution (5:10:25:167:303 10% Blocker D-R/SULFO-TAG Anti-Total ERK1/2 Antibody/2% Blocker D-M/Blocking solution/Tris wash buffer v/v) was added (25 μL) for 1 h together with vigorous shaking at room temperature. Wells were washed again with 300 μL Tris wash buffer. A reading buffer (5:15 Reading Buffer T/deionized water v/v) was added (150 μL) just before analyzing the samples with DISCOVERY WORKBENCH.

Determination of MIC against *E. coli*. The MIC values of ^{nat}Ga-labeled variants were determined via the Broth microdilution assay according to the EUCAST guidelines, which was executed in sterile 96-well polystyrene flat-bottom

https://doi.org/10.1021/acs.bioconjchem.1c00369
Bioconjugate Chem. 2021, 32, 2052−2064

microtiter plates (BD Biosciences) and previously described elsewhere.[8] In brief, a single *E. coli* colony was inoculated into 5 mL Luria−Bertani broth and grown to the end-exponential growth phase in a shaking incubator at 37 °C. Cultures were subsequently diluted to an OD600 of 0.002 (1×10^8 CFU/mL) in fresh Luria−Bertani medium. Luria−Bertani medium with peptide concentration ranging from 100 to 0.75 μg/mL were serially diluted in the 96-well plate containing bacteria solutions. Then, the 96-well plates were statically incubated overnight at 37 °C to allow bacterial growth. The absorbance of the growth bacteria was measured using a PerkinElmer spectrophotometer (1420 Multilabel Counter Victor 3).

Staining and Visualization of Inclusion Bodies of ^{nat}Ga-Labeled Variants-Treated *E. coli*. An end-exponential culture of *E. coli* was washed with PBS three times and the amount of bacteria adjusted to 10^8 cells/mL (OD600 of 0.002). Bacteria were treated with ^{nat}Ga-labeled variants at MIC or vehicle (10% DMSO in 0.9% NaCl) for 2 h. Then, the bacteria were treated with pFTAA 0.5 μM in Milli-Q water for 90 min. Finally, bacteria were imaged using structured illumination microscopy (SIM) via a LSM880 ElyraPS1SIM System (Carl Zeiss, Germany). All data were acquired using an Olympus 100× 1.46 NA objective with standard excitation and emission filter sets. For pFTAA, the absorption and emission spectra were measured from 480 to 600 nm with excitation at 440 nm (20 nm bandpass).

Fluorescence Activated Cell Sorting (FACS) Analysis of ^{nat}Ga-Labeled Variants-Treated *E. coli*. Using a double staining flow cytometry protocol with propidium iodide (PI, Invitrogen) and pFTAA, peptide uptake and killing rate were determined in a two-dimensional analysis previously described elsewhere.[8] In brief, end-exponential growth phase *E. coli* (10^8 CFU/mL) were washed with PBS and treated with ^{nat}Ga-labeled variants at MIC for different time periods, namely, 2, 3, and 6 h. Then, treated *E. coli* were washed with PBS three times and were incubated with pFTAA 0.5 μM in Milli-Q water for 90 min. PI solution was added to the bacteria, and after incubation for 5 min, the mixture was aliquoted into FACS tubes. The fluorescence intensity was measured in two channels using the Gallios Flow Cytometer, for PI excitation at 536 nm and emission at 617 nm; for pFTAA, the absorption and emission spectra were measured from 480 to 600 nm with excitation at 440 nm (20 nm bandpass). Bacteria heated at 90 °C for 10 min were used as PI-positive control.

***In Vitro* Cell Binding and Internalization Experiments.** HUVECs were plated in a 24-well plate (150,000 cells/well) precoated with 0.1% gelatin and adhered overnight at 37 °C to maximum 80% confluency. Cells were incubated with 500 kBq radiolabeled peptide dissolved in EGM2 complete medium for 30 min to 2 h at 37 °C. After incubation, cells were washed three times with 250 μL of ice-cold PBS to collect the unbound fraction and then exposed twice to 500 μL glycine-HCl in PBS (50 mM, pH 2.8) for 5 min at room temperature, to separate membrane-associated radioactivity. Cells were washed three times with 250 μL of ice-cold PBS and then lysed by adding 250 μL of lysis buffer (reagent A100, Chemometic, Allerod, Denmark). After 5 min incubation, 250 μL neutralization buffer (reagent B, Chemometic, Allerod, Denmark) was added to quench lysing of the cells. The radioactivity in the different fractions (unbound, membrane-associated, and internalized) was measured in an automated gamma counter which contained a 3 in. NaI(Tl) well crystal linked to a multichannel analyzer (Wallac 1480 Wizard, Wallac, Turku, Finland). For quantification, counts were corrected for background, counter dead time, and physical decay during counting. Results were expressed as percentage of applied radioactivity.

Biodistribution Studies. Melanoma tumor mice and *E. coli* muscle infection mice were anesthetized with 2.5% isoflurane in O_2 at a flow rate of 1 L/min and injected with 0.5−1.5 MBq of radiolabeled peptides via a tail vein. Mice were euthanized by decapitation at different time points from 2 min to 3 h after injection (n = 3−12/time point for melanoma tumor mice and n = 3−6/time point for *E. coli* muscle infection mice), blood was collected and organs of interest were excised and weighed. The radioactivity present in the tissues was measured in an automated gamma counter which contained a 3 in. NaI(Tl) well crystal linked to a multichannel analyzer (Wallac 1480 Wizard, Wallac, Turku, Finland). For quantification, counts were corrected for background, counter dead time, and physical decay during counting. Tissue and organ uptake was calculated as a percentage of injected dose (%ID, calculated as (counts per minute (cpm) in organ/total cpm recovered) × 100) and SUV (calculated as (radioactivity in cpm in organ/weight of organ in grams)/(total cpm recovered/body weight in grams)). For calculation of the total radioactivity in the blood, muscle, and bone, the masses were considered to be 7%, 40%, and 12%, respectively, of the total body mass.[60,61] In figures displaying %ID, "urine" is %ID of excreted urine and the bladder combined to represent the total urinary elimination.

***Ex Vivo* Autoradiography.** Melanoma tumor mice and *E. coli* muscle infected mice were anesthetized with isoflurane 2.5% in O_2 at a flow rate of 1 L/min, 3.5−5.5 MBq radiolabeled peptide was injected i.v. via a tail vein, and after 30 or 60 min (n = 3−4/time point), mice were euthanized by decapitation. Tumor and muscle tissues were dissected, rinsed with saline to remove blood, and snap frozen in 2-methylbutane (cooled to −40 °C). Next, 50 μm sections were obtained using a cryotome (Shandon cryotome FSE; Thermo Fisher, Waltham, MA) and mounted on adhesive microscope slides (Superfrost Plus; Thermo Fisher Scientific). The slides were exposed to phosphor storage screens (super-resolution screen; PerkinElmer, USA) for at least 12 h, screens were read in a Cyclone Plus system (PerkinElmer), and images were analyzed using Optiquant software (PerkinElmer).

Whole-Body Fluorescence Imaging. The use of GFP-expressing *E. coli* allowed to study the bacterial infection in the mice by whole-body fluorescence imaging, which was performed using the IVIS SpectrumBL *in vivo* optical imaging system. Right before imaging, the mice were euthanized by cervical dislocation and placed on a black sheet in the IVIS SpectrumBL. To achieve optimal transdermal fluorescence transmission, the fur was gently removed with a shaver and the skin covering the muscle tissue was removed as well. The images were obtained by use of the GFP filter set (excitation wavelength 491 nm, emission wavelength 509 nm).

Visualization of E. coli in Muscle Tissue Slices by SIM. Snap-frozen tissue section slides of 5 μm obtained from the same mice used for *ex vivo* autoradiography were stained with CellMask Deep Red plasma membrane dye and DAPI for SIM. Different channels were used to detect the mammalian cell membrane (laser line 555 nm), mammalian cell nucleus (laser line 405 nm), and bacterial GFP-expression (laser line 488/510 nm). Imaging was performed using a LSM880 ElyraPS1SIM System (Carl Zeiss, Germany). All data were

https://doi.org/10.1021/acs.bioconjchem.1c00369
Bioconjugate Chem. 2021, 32, 2052−2064

acquired using an Olympus 100× 1.46 NA objective with standard excitation and emission filter sets.

PET Imaging. Small animal whole body PET scans were acquired using a FOCUS 220 μPET scanner (Concorde Microsystems, Knoxville, USA). Before PET scanning, mice were anesthetized using 2.5% isoflurane in oxygen (1 l/min) and maintained under anesthesia during the entire scanning period. Immediately after IV injection of 2−3.5 MBq of radiolabeled peptide via a tail vein, mice were scanned dynamically for 3 h. Regions of interest were manually drawn and time−activity curves (TACs) of regions of interest were generated using PMOD software (v 3.3, PMOD Technologies, Zürich, Switzerland) and expressed as standardized uptake values (SUV; g/mL), decay-corrected uptake normalized for injected radioactive dose and body weight of animal, calculated as (radioactivity in target tissue in *n*Ci/mL)/(injected dose in *n*Ci/body weight in g)). Acquisition data were Fourier binned in 24 time frames (4 × 15 s, 4 × 60 s, 5 × 180 s, 8 × 300 s, 3 × 600 s). SUV value-scaled images were obtained using PMOD software. For [^{18}F]FDG, the mice were fasted overnight (only access to water), anesthetized using 2.5% isoflurane in oxygen (1 L/min), and about 11 MBq of [^{18}F]FDG was injected IV. The mice were maintained on a heating pad under anesthesia during 30 min before the PET scan was started. Mice were then subjected to a 10 min static scan, and SUV value-scaled images were obtained using PMOD software.

Statistical Analysis. All graphs and statistics were constructed in Graphpad Prism 7.01 (Graphpad Software). Quantitative data are expressed as mean ± SD. The data distribution for all experiments was checked for normality using a Shapiro−Wilk test. *P*-values were calculated using unpaired two-tailed *t* tests when comparing means between two groups. Welch's correction was used in conditions of unequal variances. One-way ANOVA was used when comparing means of more than two groups. For ANOVA, the assumption of the groups having similar standard deviations was checked by using Bartlett's test.

Supporting Information. Supplemental text on synthesis and characterization of vascin and P2 modified for radiolabeling and plasma *ex vivo* radiometabolite analysis of radiolabeled vascin and P2, and supplemental figures.

■ ASSOCIATED CONTENT

Supporting Information

The Supporting Information is available free of charge at https://pubs.acs.org/doi/10.1021/acs.bioconjchem.1c00369.

Figure showing molecular model of the P2 APR in an amyloid conformation; Figure showing ^{nat}Ga-labeled NODAGA-PEG4-vascin conserves inhibitory effect of unmodified vascin on VEGFR2; Figure showing ^{nat}Ga-labeled NODAGA-PEG2-P2 induces toxic inclusion bodies in *E. coli* leading to bacterial cell death,; Figure showing accumulation of radiolabeled P2 and ^{18}FDG in a mouse hind leg muscle infection model. Description of synthesis of vascin and P2 modified for radiolabeling. Description of plasma radiometabolite analysis. (PDF)

■ AUTHOR INFORMATION

Corresponding Authors

Joost Schymkowitz − *Switch Laboratory, VIB Center for Brain and Disease Research, Leuven, Belgium and Switch Laboratory, Department of Cellular and Molecular Medicine, KU Leuven, BE3000 Leuven, Belgium*; Phone: +32 16 37 25 73; Email: joost.schymkowitz@kuleuven.vib.be

Guy Bormans − *Laboratory for Radiopharmaceutical Research, Department of Pharmaceutical and Pharmacological Sciences, KU Leuven, BE3000 Leuven, Belgium*; orcid.org/0000-0002-0335-7190; Phone: +32 16 33 04 47; Email: guy.bormans@kuleuven.be

Frederic Rousseau − *Switch Laboratory, VIB Center for Brain and Disease Research, Leuven, Belgium and Switch Laboratory, Department of Cellular and Molecular Medicine, KU Leuven, BE3000 Leuven, Belgium*; Phone: +32 16 37 25 72; Email: frederic.rousseau@kuleuven.vib.be

Authors

Maxime Siemons − *Laboratory for Radiopharmaceutical Research, Department of Pharmaceutical and Pharmacological Sciences and Switch Laboratory, VIB Center for Brain and Disease Research, Leuven, Belgium and Switch Laboratory, Department of Cellular and Molecular Medicine, KU Leuven, BE3000 Leuven, Belgium*

Kaat Luyten − *Laboratory for Radiopharmaceutical Research, Department of Pharmaceutical and Pharmacological Sciences and Switch Laboratory, VIB Center for Brain and Disease Research, Leuven, Belgium and Switch Laboratory, Department of Cellular and Molecular Medicine, KU Leuven, BE3000 Leuven, Belgium*

Ladan Khodaparast − *Switch Laboratory, VIB Center for Brain and Disease Research, Leuven, Belgium and Switch Laboratory, Department of Cellular and Molecular Medicine, KU Leuven, BE3000 Leuven, Belgium*

Laleh Khodaparast − *Switch Laboratory, VIB Center for Brain and Disease Research, Leuven, Belgium and Switch Laboratory, Department of Cellular and Molecular Medicine, KU Leuven, BE3000 Leuven, Belgium*

Joan Lecina − *Laboratory for Radiopharmaceutical Research, Department of Pharmaceutical and Pharmacological Sciences, KU Leuven, BE3000 Leuven, Belgium*

Filip Claes − *Switch Laboratory, VIB Center for Brain and Disease Research, Leuven, Belgium and Switch Laboratory, Department of Cellular and Molecular Medicine, KU Leuven, BE3000 Leuven, Belgium*

Rodrigo Gallardo − *Switch Laboratory, VIB Center for Brain and Disease Research, Leuven, Belgium and Switch Laboratory, Department of Cellular and Molecular Medicine, KU Leuven, BE3000 Leuven, Belgium*

Michel Koole − *Nuclear Medicine and Molecular Imaging, Department of Imaging and Pathology, KU Leuven and UZ Leuven, BE3000 Leuven, Belgium*

Meine Ramakers − *Switch Laboratory, VIB Center for Brain and Disease Research, Leuven, Belgium and Switch Laboratory, Department of Cellular and Molecular Medicine, KU Leuven, BE3000 Leuven, Belgium*

Complete contact information is available at: https://pubs.acs.org/10.1021/acs.bioconjchem.1c00369

Author Contributions

M.S. performed synthesis, radiolabeling, radiological cell binding studies, *in vivo* and *ex vivo* radiological experiments and statistical analysis and provided tumor-inoculated mice. K.L. performed radiolabeling and μPET imaging experiments and provided tumor-inoculated mice. L.K. and L.K. performed bacterial experiments, whole-body fluorescence imaging,

https://doi.org/10.1021/acs.bioconjchem.1c00369
Bioconjugate Chem. 2021, 32, 2052−2064

structured illumination microscopy, and fluorescence-activated cell sorting and provided the *E. coli*-infected muscle mouse model. J.L. assisted in chemical synthesis and quality control of peptides. F.C. assisted in providing tumor-inoculated mice and data interpretation. R.G. aided in peptide design and chemical synthesis. M.K. assisted in PET data analysis and interpretation. M.R. assisted in performing ERK1/2 MSD ELISA assays. M.S., G.B., J.S., and F.R. executed study design and writing of the manuscript.

Funding

Belgian Federal Office for Scientific Affairs of Belgium (Belspo), IUAP, grant number P7/16; Flanders Agency for innovation by Science and Technology (IWT, SBO grant 60839); PhD Fellowship from the Fonds Wetenschappelijk Onderzoek Vlaanderen (FWO) (M.S.). The Switch Laboratory was supported by grants from the European Research Council under the European Union's Horizon 2020 Framework Programme ERC Grant agreement 647458 (MANGO) to J.S. KU Leuven (C2 projects C24E/19/070 & C24/17/075), the Funds for Scientific Research Flanders (FWO), the Stichting Tegen Kanker (FAF-F/201//1174), and the Flanders institute for biotechnology (V.I.B.).

Notes

The authors declare the following competing financial interest(s): JS and FR are listed as inventors of patents held by their holding institution VIB, covering the peptides described in this manuscript, and which are licensed to Aelin Therapeutics, (Leuven, Belgium), of which JS and FR are the scientific founders. All other authors declare no competing financial interests.

■ ACKNOWLEDGMENTS

The authors would like to thank Julie Cornelis for her contribution to the animal experiments, Ivan Sannen and Pieter Haspeslagh for the technical handling of HPLC and LC-MS experiments (Laboratory for Radiopharmaceutical Research), and Ann Van Santvoort, Tine Buelens, and Jens Wouters (Department of Nuclear Medicine) for the aid in the organization of and technical assistance in the animal experiments.

■ ABBREVIATIONS

APR, aggregation prone region; CFU, colony-forming unit; EPR, enhanced permeability and retention effect; ERK, extracellular signal-regulated kinase; FACS, fluorescence activated cell sorting; [^{18}F]FDG, ^{18}F-labeled 2-fluoro-2-deoxy-D-glucose; GFP, green fluorescent protein; HUVEC, human umbilical vein endothelial cells; LPS, lipopolysaccharide; MIC, minimum inhibitory concentration; MSD ELISA, mesoscale discovery enzyme-linked immuno-sorbent assay; Muscle SUVR, muscle-to-muscle SUV ratio; NODAGA, 1,4,7-triazacyclononane,1-glutaric acid-4,7-acetic acid; PET, positron emission tomography; PI, propidium iodide; SIM, structured illumination microscopy; SUV, standardized uptake value; TAC, time−activity curve; T/M SUVR, tumor-to-muscle SUV ratio; VEGF, vascular endothelial growth factor; VEGFR, vascular endothelial growth factor receptor

■ REFERENCES

(1) Sawaya, M. R.; Sambashivan, S.; Nelson, R.; Ivanova, M. I.; Sievers, S. A.; Apostol, M. I.; Thompson, M. J.; Balbirnie, M.; Wiltzius, J. J. W.; Mcfarlane, H. T.; et al. Atomic structures of amyloid cross-beta spines reveal varied steric zippers. *Nature* **2007**, *447*, 453−457.

(2) Nelson, R.; Sawaya, M. R.; Balbirnie, M.; Madsen, A. Ø.; Riekel, C.; Grothe, R.; Eisenberg, D. Structure of the cross-beta spine of amyloid-like fibrils. *Nature* **2005**, *435*, 773−778.

(3) Ganesan, A.; Debulpaep, M.; Wilkinson, H.; Van Durme, J.; De Baets, G.; Jonckheere, W.; Ramakers, M.; Ivarsson, Y.; Zimmermann, P.; Van Eldere, J.; Schymkowitz, J.; Rousseau, F. Selectivity of Aggregation-Determining Interactions. *J. Mol. Biol.* **2015**, *427*, 236−247.

(4) Chiti, F.; Dobson, C. M. Protein Misfolding, Functional Amyloid, and Human Disease. *Annu. Rev. Biochem.* **2006**, *75*, 333−366.

(5) Perchiacca, J. M.; Ladiwala, A. R. A.; Bhattacharya, M.; Tessier, P. M. Structure-based design of conformation- and sequence-specific antibodies against amyloid. *Proc. Natl. Acad. Sci. U. S. A.* **2012**, *109*, 84−89.

(6) Schonhoft, J. D.; Monteiro, C.; Plate, L.; Eisele, Y. S.; Kelly, J. M.; Boland, D.; Parker, C. G.; Cravatt, B. F.; Teruya, S.; Helmke, S.; et al. Peptide probes detect misfolded transthyretin oligomers in plasma of hereditary amyloidosis patients. *Sci. Transl. Med.* **2017**, *9*, No. eaam7621.

(7) Betti, C.; Vanhoutte, I.; Coutuer, S.; De Rycke, R. M.; Mishev, K.; Vuylsteke, M.; Aesaert, S.; Rombaut, D.; Gallardo, R.; De Smet, F.; Xu, J.; Van Lijsebettens, M.; Van Breusegem, F.; Inze, D.; Rousseau, F.; Schymkowitz, J.; Russinova, E.; et al. Sequence-specific protein aggregation generates defined protein knockdowns in plants. *Plant Physiol.* **2016**, *171*, 773−787.

(8) Khodaparast, L.; Khodaparast, L.; Gallardo, R.; Louros, N. N.; Michiels, E.; Ramakrishnan, R.; Ramakers, M.; Claes, F.; Young, L.; Shahrooei, M.; et al. Aggregating sequences that occur in many proteins constitute weak spots of bacterial proteostasis. *Nat. Commun.* **2018**, *9*, 1−15.

(9) Bednarska, N. G.; van Eldere, J.; Gallardo, R.; Ganesan, A.; Ramakers, M.; Vogel, I.; Baatsen, P.; Staes, A.; Goethals, M.; Hammarstrom, P.; Nilsson, K. P. R.; Gevaert, K.; Schymkowitz, J.; Rousseau, F. Protein aggregation as an antibiotic design strategy. *Mol. Microbiol.* **2016**, *99*, 849−865.

(10) Michiels, E.; Roose, K.; Gallardo, R.; Khodaparast, L.; Khodaparast, L.; van der Kant, R.; Siemons, M.; Houben, B.; Ramakers, M.; Wilkinson, H.; et al. Reverse engineering synthetic antiviral amyloids. *Nat. Commun.* **2020**, *11*, 1−13.

(11) Gallardo, R.; Ramakers, M.; de Smet, F.; Claes, F.; Khodaparast, L.; Khodaparast, L.; Couceiro, J. R.; Langenberg, T.; Siemons, M.; Nystrom, S.; et al. De novo design of a biologically active amyloid. *Science* **2016**, *354*, No. aah4949.

(12) Rousseau, F.; Serrano, L.; Schymkowitz, J. W. H. How Evolutionary Pressure Against Protein Aggregation Shaped Chaperone Specificity. *J. Mol. Biol.* **2006**, *355*, 1037−1047.

(13) Goldschmidt, L.; Teng, P. K.; Riek, R.; Eisenberg, D. Identifying the amylome, proteins capable of forming amyloid-like fibrils. *Proc. Natl. Acad. Sci. U. S. A.* **2010**, *107*, 3487−3492.

(14) Ametamey, S. M.; Honer, M.; Schubiger, P. A. Molecular Imaging with PET. *Chem. Rev.* **2008**, *108*, 1501−1516.

(15) Phelps, M. E. Positron emission tomography provides molecular imaging of biological processes. *Proc. Natl. Acad. Sci. U. S. A.* **2000**, *97*, 9226−9233.

(16) Perchiacca, J. M.; Ladiwala, A. R. A.; Bhattacharya, M.; Tessier, P. M. Structure-based design of conformation- and sequence-specific antibodies against amyloid *β*. *Proc. Natl. Acad. Sci. U. S. A.* **2012**, *109*, 84−89.

(17) Couceiro, J. R.; Gallardo, R.; De Smet, F.; De Baets, G.; Baatsen, P.; Annaert, W.; Roose, K.; Saelens, X.; Schymkowitz, J.; Rousseau, F. Sequence-dependent Internalization of Aggregating Peptides. *J. Biol. Chem.* **2015**, *290*, 242−258.

(18) Forrer, F.; Valkema, R.; Kwekkeboom, D. J.; de Jong, M.; Krenning, E. P. Peptide receptor radionuclide therapy. *Best Pract. Res., Clin. Endocrinol. Metab.* **2007**, *21*, 111−129.

https://doi.org/10.1021/acs.bioconjchem.1c00369
Bioconjugate Chem. 2021, 32, 2052−2064

(19) Solnes, L. B.; Werner, R. A.; Jones, K. M.; Sadaghiani, M. S.; Bailey, C. R.; Lapa, C.; Pomper, M. G.; Rowe, S. P. Theranostics: leveraging molecular imaging and therapy to impact patient management and secure the future of nuclear medicine. *J. Nucl. Med.* **2020**, *61*, 311−318.
(20) Fernandez-Escamilla, A.-M.; Rousseau, F.; Schymkowitz, J.; Serrano, L. Prediction of sequence-dependent and mutational effects on the aggregation of peptides and proteins. *Nat. Biotechnol.* **2004**, *22*, 1302−1306.
(21) De Baets, G.; Van Durme, J.; Rousseau, F.; Schymkowitz, J. A genome-wide sequence-structure analysis suggests aggregation gatekeepers constitute an evolutionary constrained functional class. *J. Mol. Biol.* **2014**, *426*, 2405−2412.
(22) Beerten, J.; Jonckheere, W.; Rudyak, S.; Xu, J.; Wilkinson, H.; De Smet, F.; Schymkowitz, J.; Rousseau, F. Aggregation gatekeepers modulate protein homeostasis of aggregating sequences and affect bacterial fitness. *Protein Eng., Des. Sel.* **2012**, *25*, 357−366.
(23) Khodaparast, L.; Khodaparast, L.; Gallardo, R.; Louros, N. N.; Michiels, E.; Ramakrishnan, R.; Ramakers, M.; Claes, F.; Young, L.; Shahrooei, M.; et al. Aggregating sequences that occur in many proteins constitute weak spots of bacterial proteostasis. *Nat. Commun.* **2018**, *9*, 1−15.
(24) Aslund, A.; Sigurdson, C. J.; Klingstedt, T.; Grathwohl, S.; Bolmont, T.; Dickstein, D. L.; Glimsdal, E.; Prokop, S.; Lindgren, M.; Konradsson, P.; Holtzman, D. M.; Hof, P. R.; Heppner, F. L.; Gandy, S.; Jucker, M.; Aguzzi, A.; Hammarstrom, P.; Nilsson, K. P. R. Novel Pentameric Thiophene Derivatives for in Vitro and in Vivo Optical Imaging of a Plethora of Protein Aggregates in Cerebral Amyloidoses. *ACS Chem. Biol.* **2009**, *4*, 673−684.
(25) Hancock, R. E. W.; Chapple, D. S. Peptide Antibiotics. *Antimicrob. Agents Chemother.* **1999**, *43*, 1317−1323.
(26) Gunnoo, S. B.; Madder, A. Bioconjugation - using selective chemistry to enhance the properties of proteins and peptides as therapeutics and carriers. *Org. Biomol. Chem.* **2016**, *14*, 8002−8013.
(27) Vegt, E.; van Eerd, J. E. M.; Eek, a.; Oyen, W. J. G.; Wetzels, J. F. M.; de Jong, M.; Russel, F. G. M.; Masereeuw, R.; Gotthardt, M.; Boerman, O. C. Reducing Renal Uptake of Radiolabeled Peptides Using Albumin Fragments. *J. Nucl. Med.* **2008**, *49*, 1506−1511.
(28) Vegt, E.; de Jong, M.; Wetzels, J. F.M.; Masereeuw, R.; Melis, M.; Oyen, W. J.G.; Gotthardt, M.; Boerman, O. C. Renal Toxicity of Radiolabeled Peptides and Antibody Fragments: Mechanisms, Impact on Radionuclide Therapy, and Strategies for Prevention. *J. Nucl. Med.* **2010**, *51*, 1049−1059.
(29) Wood, J. M.; Bold, G.; Buchdunger, E.; Cozens, R.; Ferrari, S.; Hofmann, F.; Mett, H.; Reilly, T. O.; Persohn, E.; Ro, J.; et al. PTK787/ZK 222584, a Novel and Potent Inhibitor of Vascular Endothelial Growth Factor Receptor Tyrosine Kinases, Impairs Vascular Endothelial Growth Factor- induced Responses and Tumor Growth after Oral Administration. *Cancer Res.* **2000**, *60*, 2178−2189.
(30) Iyer, A. K.; Khaled, G.; Fang, J.; Maeda, H. Exploiting the enhanced permeability and retention effect for tumor targeting. *Drug Discovery Today* **2006**, *11*, 812−818.
(31) Kumar, V.; Boddeti, D. K. (68)Ga-radiopharmaceuticals for PET imaging of infection and inflammation. *Recent Results Cancer Res.* **2013**, *194*, 189−219.
(32) van Oosten, M.; Hahn, M.; Crane, L. M.A.; Pleijhuis, R. G.; Francis, K. P.; van Dijl, J. M.; van Dam, G. M. Targeted imaging of bacterial infections: advances, hurdles and hopes. *FEMS Microbiol. Rev.* **2015**, *39*, 892−916.
(33) Bunschoten, A.; Welling, M. M.; Termaat, M. F.; Sathekge, M.; van Leeuwen, F. W. B. Development and Prospects of Dedicated Tracers for the Molecular Imaging of Bacterial Infections. *Bioconjugate Chem.* **2013**, *24*, 1971−1989.
(34) Glaudemans, A. W. J. M.; Israel, O.; Slart, R. H. J. A. Pitfalls and Limitations of Radionuclide and Hybrid Imaging in Infection and Inflammation. *Semin. Nucl. Med.* **2015**, *45*, 500−512.
(35) Altini, C.; Ferrari, C.; Rubini, G. Multimodality Imaging in Tumor Angiogenesis: Present Status and Perspectives. *Int. J. Mol. Sci.* **2017**, *18*, 1864.
(36) Taurone, S.; Galli, F.; Signore, A.; Agostinelli, E.; Dierckx, R. A. J. O.; Minni, A.; Pucci, M.; Artico, M. VEGF in nuclear medicine: Clinical application in cancer and future perspectives (Review). *Int. J. Oncol.* **2016**, *49*, 437−447.
(37) Provost, C.; Prignon, A.; Cazes, A.; Combaret, V.; Delattre, O.; Janoueix-Lerosey, I.; Montravers, F.; Talbot, J.; Imaging, M. 68Ga-DOTATOC and FDG PET Imaging of Preclinical Neuroblastoma Models. *Anticancer Res.* **2016**, *36*, 4459−4466.
(38) Zolghadri, S.; Naderi, M.; Hassan, Y.; Behrouz, A.; Beiki, D. Evaluation of the Possible Utilization of 68Ga-DOTATOC in Diagnosis of Adenocarcinoma Breast Cancer. *Asia Ocean. J. Nucl. Med. Biol.* **2018**, *6*, 41.
(39) Soto-Montenegro, M. L.; Peña-Zalbidea, S.; Mateos-Pérez, J. M.; Oteo, M.; Romero, E.; Morcillo, M.Á.; Desco, M. Meningiomas: A comparative study of 68Ga-DOTATOC, 68Ga-DOTANOC and 68Ga-DOTATATE for molecular imaging in mice. *PLoS One* **2014**, *9*, e111624.
(40) Wang, H.; Cai, W.; Chen, K.; Li, Z.; Kashefi, A.; He, L.; Chen, X. A new PET tracer specific for vascular endothelial growth factor receptor 2. *Eur. J. Nucl. Med. Mol. Imaging* **2007**, *34*, 2001−2010.
(41) Eder, M.; Krivoshein, A. V.; Backer, M.; Backer, J. M.; Haberkorn, U.; Eisenhut, M. ScVEGF-PEG-HBED-CC and scVEGF-PEG-NOTA conjugates: comparison of easy-to-label recombinant proteins for [68Ga] PET imaging of VEGF receptors in angiogenic vasculature. *Nucl. Med. Biol.* **2010**, *37*, 405−412.
(42) Kang, C. M.; Kim, S.; Koo, H.; Yim, M. S.; Lee, K.; Ryu, E. K. In vivo characterization of 68 Ga-NOTA-VEGF 121 for the imaging of VEGF receptor expression in U87MG tumor xenograft models. *Eur. J. Nucl. Med. Mol. Imaging* **2013**, *40*, 198−206.
(43) Backer, M. V.; Levashova, Z.; Patel, V.; Jehning, B. T.; Claffey, K.; Blankenberg, F. G.; Backer, J. M. Molecular imaging of VEGF receptors in angiogenic vasculature with single-chain VEGF-based probes. *Nat. Med.* **2007**, *13*, 504−509.
(44) Zolghadri, S.; Naderi, M.; Hassan, Y.; Behrouz, A.; Beiki, D. Evaluation of the Possible Utilization of 68Ga-DOTATOC in Diagnosis of Adenocarcinoma Breast Cancer. *Asia Ocean. J. Nucl. Med. Biol.* **2018**, *6*, 41.
(45) Blankenberg, F. G.; Backer, M. V.; Levashova, Z.; Patel, V.; Backer, J. M. In vivo tumor angiogenesis imaging with site-specific labeled Tc-HYNIC-VEGF. *Eur. J. Nucl. Med. Mol. Imaging* **2006**, *33*, 841−848.
(46) Cai, W.; Chen, K.; Mohamedali, K. A.; Cao, Q.; Gambhir, S. S.; Rosenblum, M. G.; Chen, X. PET of Vascular Endothelial Growth Factor Receptor Expression. *J. Nucl. Med.* **2006**, *47*, 2048−2056.
(47) Luo, H.; England, C. G.; Graves, S. a.; Sun, H.; Liu, G.; Nickles, R. J.; Cai, W. PET Imaging of VEGFR-2 Expression in Lung Cancer with 64Cu-Labeled Ramucirumab. *J. Nucl. Med.* **2016**, *57*, 285−290.
(48) Weinstein, E. a.; Ordonez, a. a.; DeMarco, V. P.; Murawski, a. M.; Pokkali, S.; MacDonald, E. M.; Klunk, M.; Mease, R. C.; Pomper, M. G.; Jain, S. K. Imaging Enterobacteriaceae infection in vivo with 18F-fluorodeoxysorbitol positron emission tomography. *Sci. Transl. Med.* **2014**, *6*, 259ra146.
(49) Ning, X.; Seo, W.; Lee, S.; Takemiya, K.; Rafi, M.; et al. Fluorine-18 labeled maltohexaose images bacterial infections by PET. *Angew. Chem., Int. Ed.* **2014**, *53*, 14096−14101.
(50) Wang, X.; Murthy, N. Bacterial Imaging Comes of Age. *Sci. Transl. Med.* **2014**, *6*, 1−4.
(51) Weinstein, E. a.; Ordonez, a. a.; DeMarco, V. P.; Murawski, a. M.; Pokkali, S.; MacDonald, E. M.; Klunk, M.; Mease, R. C.; Pomper, M. G.; Jain, S. K. Imaging Enterobacteriaceae infection in vivo with 18F-fluorodeoxysorbitol positron emission tomography. *Sci. Transl. Med.* **2014**, *6*, 259ra146.
(52) Martínez, M. E.; Kiyono, Y.; Noriki, S.; Inai, K.; Mandap, K. S.; Kobayashi, M.; Mori, T.; Tokunaga, Y.; Tiwari, V. N.; Okazawa, H.; et al. New radiosynthesis of 2-deoxy-2-[18F]fluoroacetamido-d-

https://doi.org/10.1021/acs.bioconjchem.1c00369
Bioconjugate Chem. 2021, 32, 2052−2064

glucopyranose and its evaluation as a bacterial infections imaging agent. *Nucl. Med. Biol.* **2011**, *38*, 807−817.
(53) Ning, X.; Seo, W.; Lee, S.; Takemiya, K.; Rafi, M.; Feng, X.; Weiss, D.; Wang, X.; Williams, L.; Camp, V. M.; et al. PET Imaging of Bacterial Infections with Fluorine-18-Labeled Maltohexaose. *Angew. Chem., Int. Ed.* **2014**, *53*, 14096−14101.
(54) Gowrishankar, G.; Namavari, M.; Jouannot, E. B.; Hoehne, A.; Reeves, R.; Hardy, J.; Gambhir, S. S. Investigation of 6-[18F]-Fluoromaltose as a Novel PET Tracer for Imaging Bacterial Infection. *PLoS One* **2014**, *9*, 6−11.
(55) Zhang, Z.; Ordonez, A. A.; Wang, H.; Li, Y.; Gogarty, K. R.; Weinstein, E. A.; Daryaee, F.; Merino, J.; Yoon, G. E.; Kalinda, A. S.; et al. Positron Emission Tomography Imaging with 2 -[18F]F-p-Aminobenzoic Acid Detects Staphylococcus aureus Infections and Monitors Drug Response. *ACS Infect. Dis.* **2018**, *4*, 1635−1644.
(56) Vilche, M. B.; Reyes, A. L.; Vasilskis, E.; Oliver, P.; Balter, H. S.; Engler, H. W. 68Ga-NOTA-UBI 29−41 as a PET tracer for detection of bacterial infection. *J. Nucl. Med.* **2016**, *57*, 622−627.
(57) Sellmyer, M. a.; Lee, I.; Hou, C.; Weng, C.-C.; Li, S.; Lieberman, B. P.; Zeng, C.; Mankoff, D. a.; Mach, R. H. Bacterial infection imaging with [^{18}F]fluoropropyl-trimethoprim. *Proc. Natl. Acad. Sci. U. S. A.* **2017**, *114*, 8372−8377.
(58) Martínez, M. E.; Kiyono, Y.; Noriki, S.; Inai, K.; Mandap, K. S.; Kobayashi, M.; Mori, T.; Tokunaga, Y.; Tiwari, V. N.; Okazawa, H.; et al. New radiosynthesis of 2-deoxy-2-[18F]fluoroacetamido-d-glucopyranose and its evaluation as a bacterial infections imaging agent. *Nucl. Med. Biol.* **2011**, *38*, 807−817.
(59) Vilche, M. B.; Reyes, A. L.; Vasilskis, E.; Oliver, P.; Balter, H. S.; Engler, H. W. 68Ga-NOTA-UBI 29−41 as a PET tracer for detection of bacterial infection. *J. Nucl. Med.* **2016**, *57*, 622−627.
(60) Burns, H. D.; Van Laere, K.; Sanabria-Bohorquez, S.; Hamill, T. G.; Bormans, G.; Eng, W. -s.; Gibson, R.; Ryan, C.; Connolly, B.; Patel, S.; et al. [18F]MK-9470, a positron emission tomography (PET) tracer for in vivo human PET brain imaging of the cannabinoid-1 receptor. *Proc. Natl. Acad. Sci. U. S. A.* **2007**, *104*, 9800−9805.
(61) Horti, a G.; Fan, H.; Kuwabara, H.; Hilton, J.; Ravert, H. T.; Holt, D. P.; Alexander, M.; Kumar, a; Rahmim, a; Scheffel, U.; et al. 11C-JHU75528: a radiotracer for PET imaging of CB1 cannabinoid receptors. *J. Nucl. Med.* **2006**, *47*, 1689−1696.

https://doi.org/10.1021/acs.bioconjchem.1c00369
Bioconjugate Chem. 2021, 32, 2052−2064